

Hysteresis of two-dimensional flows around a NACA0012 airfoil at $Re = 5000$ and linear analyses of their mean flow.

O. Marquet^{a,*}, J.S. Leontini^b, J. Zhao^c, M.C. Thompson^c

^a ONERA-DAAA, Paris Saclay University, 92190 Meudon, France

^b Swinburne University of Technology, Hawthorn, Victoria 3122, Australia

^c Fluids Laboratory for Aeronautical and Industrial Research (FLAIR), Department of Mechanical and Aerospace Engineering, Monash University, Melbourne, VIC 3800, Australia

ARTICLE INFO

Keywords:

Flow hysteresis
Resolvent analysis
NACA0012 airfoil
Multiple states

ABSTRACT

Two-dimensional numerical simulations of the flow around a NACA0012 profile at Reynolds number $Re = 5000$ show that unsteady periodic flows reach different saturated states when increasing or decreasing the angle of attack between 7° and 8° . Within this range, the lift signal shows co-existing periodic states and period-doubling, as the wake undergoes a substantial change in character from the standard von-Kármán vortex street. Results of experiments in a water channel also indicate a change of the flow topology but at slightly lower angles of attack $\alpha = 6^\circ$. A discussion of the discrepancy between numerical and experimental results is proposed in light of results about the three-dimensional transition of wake flows behind bluff bodies and airfoils. Finally, eigenvalue and resolvent analyses of time-averaged flows are used to investigate the two-dimensional transitions further. While a peak of energetic amplification is obtained at the frequency of a single periodic state, a double peak is observed for co-existing periodic states, the second one being at the frequency of the periodic state not used to compute the time-averaged flow. This behaviour also characterizes the resolvent analysis of the period-doubled states, although less pronounced.

1. Introduction

The aerodynamics of airfoils operating on the condition of ultra-low chord-based Reynolds number $Re \leq 10^4$ has gained increasing interest in the last ten years due to the development of Nano-Air Vehicles (Petricca et al., 2011). Compared to the low Reynolds number regime ($10^4 < Re \leq 3.5 \cdot 10^5$) that is of interest when designing Micro-Air Vehicles (Mueller and DeLaurier, 2003), the aerodynamic performance is significantly reduced. The maximal value of the time-averaged lift coefficient is decreased and occurs at significantly larger angles of attack, around $\alpha = 40^\circ$ for a NACA0012 profile at $Re = 5300$ (Wang et al., 2014). The stall phenomenon, i.e. the abrupt decrease of lift, is not even visible (Alam et al., 2010) while it occurs around $\alpha = 10^\circ$ for a NACA0012 airfoil in the low Reynolds number flow regime ($Re > 10^4$). The evolution of the time-averaged aerodynamic coefficients is related to the unsteady flow dynamics that changes drastically. The shear-layer transition does not occur close to the airfoil but further downstream in the wake. This delayed transition prevents from the formation of a (time-

averaged) laminar separation bubble that is classically observed on airfoil operating at low Reynolds number ($10^4 < Re \leq 3.5 \cdot 10^5$) and is responsible for an increased lift. In the last ten years, several studies have thus investigated the unsteady flow dynamics around a NACA0012 airfoil at these ultra-low Reynolds numbers. Experimental characterization of unsteady flow structures was performed for $Re = 1200$ (Huang et al., 2001), $Re = 3195$ (Huang and Lin, 1995) and $Re \geq 5300$ (Alam et al., 2010; Zhou et al., 2011; Wang et al., 2014). The separating shear layers, vortex formation and shedding frequency were carefully analyzed for $Re \geq 5300$ and $\alpha > 10^\circ$ based on aerodynamic force and optical flow measurements (Alam et al., 2010). In the present investigation, we are interested in better characterizing flow regimes occurring at a similar Reynolds number $Re = 5000$ but for lower angles of attack $\alpha < 10^\circ$.

In the early nineties, two-dimensional numerical simulations of the Navier–Stokes equations were performed at the angle $\alpha = 20^\circ$ (Pulliam and Vastano, 1993). By varying the Reynolds number in the range $500 \leq Re \leq 3000$, the authors identified a succession of period-doubling

* Corresponding author.

E-mail addresses: olivier.marquet@onera.fr (O. Marquet), jleontini@swin.edu.au (J.S. Leontini), jisheng.zhao@monash.edu (J. Zhao), mark.thompson@monash.edu (M.C. Thompson).

<https://doi.org/10.1016/j.ijheatfluidflow.2021.108920>

Received 15 June 2021; Received in revised form 16 November 2021; Accepted 20 December 2021

Available online 8 January 2022

0142-727X/© 2022 Elsevier Inc. All rights reserved.

bifurcation leading to chaos for the largest value of Re . Later on, two-dimensional flow simulations were performed at the Reynolds number $Re = 1000$ (Kurtulus, 2016). Varying the angle of attack by step of $\Delta\alpha = 0.5^\circ$, various flow regimes were identified in the range $0^\circ \leq \alpha \leq 30^\circ$. In particular, a transition from a periodic vortex-shedding to a periodic shedding of vortex pairs was identified around $\alpha \sim 20^\circ$. The first objective of the present paper is to reinvestigate the bifurcations of the two-dimensional wake flow behind a NACA0012 but for the larger Reynolds number $Re = 5000$ and in a restricted range of angles $6.5^\circ \leq \alpha \leq 8.5^\circ$. Unlike studies previously cited, a continuation of the solutions identified in that range of angles will be systematically performed so as to identify and characterize flow hysteresis.

The idea of analyzing the flow fluctuations from the knowledge of the time-averaged flows traces back to the late fifties (Malkus, 1956; Stuart, 1958). It was proposed that the mean flow, which results itself from the nonlinear interaction between fluctuations via the Reynolds stress tensor, could mainly be responsible for the saturation of fluctuations to finite-amplitude. This idea reemerged at the beginning of the century (Barkley, 2006) by investigating the long term dynamics of perturbations developing around the mean flow without any external force to sustain it. By performing an eigenvalue analysis of the mean flow obtained from the periodic vortex-shedding in the wake of a circular cylinder (Barkley, 2006), the authors found a slightly unstable mode whose frequency accurately predicts the vortex-shedding frequency. This marginal stability of the leading eigenmode computed with a mean flow was further discussed in (Sipp and Lebedev, 2007; Turton et al., 2015). It also led to the development of a self-consistent nonlinear model (Mantić-Lugo et al., 2015) that reconstructs the Reynolds stress tensor in the mean flow equations but neglects the interaction between harmonics in the fluctuation equations. If the eigenvalue analysis is appropriate for investigating wake flows or cavity flows whose unsteadiness is characterized by a single dominant frequency, it cannot be used to noise amplifier flows that are characterized by a broadband frequency spectrum. To capture convective instabilities that grow on spatially developing steady flows, it was proposed in Sipp et al. (2010) to determine the optimal forcing/response mode corresponding to the singular value modes of the linearized Navier–Stokes equations. Such analysis, not called a resolvent analysis (of the base flow) at that time, was performed to determine Kelvin Helmholtz instabilities developing over a separated boundary layer flow (Alizard et al., 2009), a backward-facing step flow (Marquet and Sipp, 2010; Marquet and Sipp, 2012) or the Tollmien-Schlichting waves in a laminar boundary layer (Sipp and Marquet, 2013). The idea of a self-consistent model was further extended to such noise amplifier flows (Mantić-Lugo and Gallaire, 2016) by reconstructing the fluctuations around the (laminar) mean flow based on a resolvent analysis.

In the context of turbulent flows where the frequency spectrum of fluctuations is much wider, the mean-flow resolvent analysis was introduced in McKeon and Sharma (2010) to reconstruct the fluctuations developing around a statistically turbulent mean flow. When the first singular value of the resolvent operator is several orders of magnitude larger than the rest (Beneddine et al. (2017)), the knowledge of this first resolvent mode allows to well reconstruct the fluctuations without a priori knowledge of the forcing term describing the nonlinear interaction. Resolvent analysis was applied to airfoil's flows mainly in the low Reynolds number regime $10^4 \leq Re \leq 3 \cdot 10^5$ (Symon et al., 2019; Thomareis and Papadakis, 2018; Yeh and Taira, 2019) and more recently at the larger Reynolds number $Re = 500000$ (Yeh et al., 2020). In all of these studies, the mean flow was obtained by averaging in time and space (in the spanwise homogeneous direction) the three-dimensional unsteady flow velocity computed with direct or large-eddy numerical simulations. The identification and reconstruction of two-dimensional fluctuations was investigated in Thomareis and Papadakis (2018) for a NACA0012 airfoil at $Re = 50000$ and $\alpha = 5^\circ$, and in Symon et al. (2019) for a NACA0018 airfoil at $Re = 10250$ and angles $\alpha = 0^\circ$ and $\alpha = 10^\circ$. The reconstruction of three-dimensional

fluctuations around a NACA0012 airfoil at $Re = 23500$ was investigated in Yeh and Taira (2019) for two angles $\alpha = 6^\circ$ and $\alpha = 9^\circ$. In the present paper, we will also apply the resolvent analysis but to mean flows that are computed by time-averaging two-dimensional flow solutions. Only the reconstruction of the two-dimensional perturbations will be investigated here.

The paper is organized as follows. Two-dimensional numerical flow simulations are performed in §2 showing that the wake undergoes a series of transitions over a small α range. These numerical results are then briefly compared to experimental results. In §3, resolvent analysis of the time-averaged flow is performed to analyze the co-existing periodic flow solutions over that small range of angle.

2. Characterization of unsteady flows

Unsteady flow around a NACA0012 profile of chord c immersed in a uniform upstream flow of velocity U_∞ is investigated for a fixed Reynolds number of $Re = U_\infty c / \nu = 5000$ over the angle-of-attack range $5^\circ \leq \alpha \leq 9^\circ$. Results of two-dimensional numerical simulations and water-channel experiments are described in §2.1 and §2.2, respectively.

2.1. Two-dimensional numerical simulations

The incompressible flow is described through the non-dimensional velocity u and kinematic pressure p fields that satisfy the Navier–Stokes equations

$$\frac{\partial u}{\partial t} + (u \cdot \nabla)u = -\nabla p + \frac{1}{Re} \Delta u, \quad \nabla \cdot u = 0, \quad (1)$$

where $Re = U_\infty c / \nu$ is the Reynolds number based on the chord c of a NACA0012 profile and the incoming uniform velocity is U_∞ . The equations are discretised in space using a finite-element method and marched in time with an implicit temporal discretisation. A second-order extrapolation of the convective velocity in the non-linear term yields a linear Oseen problem (John, 2016) that is solved here using a direct sparse LU solver. Denoting α as the angle-of-attack, the above equations are solved subject to Dirichlet boundary conditions $(u, v) = (\cos(\alpha), \sin(\alpha))$ at the inlet and lateral boundaries of the computational domain. The domain size is $10c$ in each direction. A free-stress boundary condition is imposed at the outlet. Flow solutions have been computed for the Reynolds number of $Re = 5000$ and several values of the angle-of-attack in the range $5^\circ \leq \alpha \leq 9^\circ$. For all simulations performed, the integration time is systematically adapted so as to reach the asymptotic flow state. As a validation check, the flows were also simulated using an independent spectral-element code (Thompson et al., 2006). Several branches of periodic solutions were identified, as described below, using both codes. The bifurcations were predicted to within a few percent; noting slight differences in the blockage ratios of the domains.

To identify various branches of solutions that may coexist in a same range of angles α , we proceed as follow. First, unsteady solutions are computed for several values of the angle-of-attack in the range $5^\circ \leq \alpha \leq 9^\circ$ starting from a uniform velocity field as an initial condition. These preliminary computations reveal in our case the existence of four types of periodic solutions, reported hereinafter, that are classified according to the time-averaged value and the period of the lift coefficient. Secondly, to determine the range of α for which each types of solution is obtained, we adopt a continuation strategy. Starting from a periodic solution at a given angle α_0 that is representative of a branch, we perform new simulations at the angle $\alpha_0 + \Delta\alpha$ (or $\alpha_0 - \Delta\alpha$). The integration time is adapted so as to ensure the convergence of the unsteady solution towards an asymptotic state. If the time-averaged value and the period of the lift coefficient are similar to the solutions at the previous angle α_0 , the solutions at the new angle $\alpha_0 + \Delta\alpha_0$ (or $\alpha_0 - \Delta\alpha_0$) belong to the branch and we repeat that procedure until the identified asymptotic state does not correspond to the followed branch. To properly identify

the switch between different branches, the step angle is adapted and may be as small as $\Delta\alpha = 0.01^\circ$.

The time-averaged $\langle C_L \rangle$ and period T of the lift coefficient are displayed as a function of angle-of-attack in Figs. 1(a) and (b), respectively. Four branches of periodic solutions are identified in the range $6.5^\circ \leq \alpha \leq 9^\circ$, based on the time-averaged value and the period of the lift coefficient. All of these solutions being periodic, we decided to only report their period in that figure. However, their frequency spectrum may not be necessarily monochromatic, as discussed below. For the first branch of solutions (black circles), the mean lift coefficient increases with the angle-of-attack until $\alpha = 7.78^\circ$, where the branch ceases to exist. A typical snapshot of the vorticity field is displayed in Fig. 2(a) for $\alpha = 6.5^\circ$. A von-Kármán vortex street is observed in the wake of the foil, with clockwise (blue) and anti-clockwise (red) vortices that are periodically shed at the trailing edge. The period of this shedding is equal to $T = tU_\infty/c = 0.6$ and barely changes with α . The frequency spectrum of the lift coefficient, displayed in Fig. 3(a), is characteristic of a monochromatic signal, with a peak at the fundamental (lowest) frequency $f_1 = 1/T = 1.65$ that is three orders of magnitude larger than the second-harmonic peak. The temporal fluctuation of the aerodynamic coefficients induced by vortex shedding is shown in Fig. 2(d), by displaying the instantaneous lift ($C_L(t)$) as a function of the instantaneous drag ($C_D(t)$). The trajectory approximates a straight line for the angle $\alpha = 6.5^\circ$ (black curve).

When increasing the angle-of-attack above $\alpha = 8^\circ$, we obtain a second branch of periodic solutions shown by the blue circles in Fig. 1, characterised by a mean lift coefficient increasing linearly with α . The temporal evolution of the aerodynamic coefficients in Fig. 2(d) now resembles an ellipse and shows that the fluctuations are of larger amplitude. The period of the lift oscillation is also larger, with $T \sim 0.8$, and this oscillation is monochromatic, as seen in Fig. 3(c). The vortex street displayed in Fig. 2(c) has deviated upwards and the distance between two vortex pairs (solid line) is larger than the distance between the two counter-rotating vortices (dashed line), unlike the situation for the classical vortex street in Fig. 2(a). This second periodic solution branch exists for large α , with the period increasing to $T = 0.9$ for $\alpha = 9^\circ$, but it ceases to exist for angles below $\alpha = 8^\circ$.

A third branch of periodic solution (red circles in Fig. 1) is obtained in the range $7.33^\circ < \alpha \leq 7.5^\circ$. The pattern of the vortex street (Fig. 2(b)) has now deviated downwards. The vortex shedding at period $T = 0.75$ is characterised by lower lift and drag coefficients, as well as fluctuations of smaller amplitude oscillation compared with the second branch (blue).

Finally, for intermediate values of angle-of-attack, $7.5^\circ < \alpha \leq 8^\circ$, we

obtain a branch of solutions (green circles in Fig. 1) characterised by much larger periods in the range $1.5 \leq T \leq 1.6$. The maximal (resp. minimal) value of the period on the green branch is twice the period of the blue (resp. red) branch equal to $T = 0.8$ (resp. 0.75). Examining the frequency spectrum in Fig. 3(b), we first note that all the peaks are obtained at frequencies that are multiple of the lowest frequency $f_1 = 1/T$. Therefore, the lift coefficient is still periodic, but not monochromatic anymore. Interestingly, the peak at the lowest frequency f_1 is actually of lower amplitude than that at $2f_1$. This suggests that the T -periodic solutions may arise from a subharmonic instability of the $T/2$ -periodic base flow, similar to the subharmonic instability that gives rise to vortex pairing in jet flows (Shaabani-Ardali et al., 2017). The trajectory of this T -periodic solution in the lift-versus-drag diagram is now displayed in Fig. 2(e) with the green curve. It looks like two connected ellipses, as if the trajectories of the first (black dashed line) and second (red dashed line) branches of periodic solutions have merged, giving birth to a new periodic solution. The instantaneous vorticity is shown in Fig. 2(f) and 2(g) for two instants corresponding to the two maximal values of the lift. The vortex pattern is clearly less organised than for the other branches of solution.

2.2. Experimental results and comparison

The experiments were conducted in the free-surface recirculating water channel of the *Fluids Laboratory for Aeronautical and Industrial Research* (FLAIR) at Monash University. A machined aluminium NACA0012 airfoil model had a chord length of $c = 30 \pm 0.010$ mm and an immersed length of $L = 300$ mm, giving an aspect ratio of $L/c = 10$. The airfoil was attached to a micro-stepping motor, allowing the angle-of-attack to be set to within $\pm 0.2^\circ$. The opposite free end of the foil was positioned with a clearance of ~ 1 mm above a conditioning platform to reduce end effects. The flow structure around the foil was measured using Particle Image Velocimetry (PIV). The mean lift coefficient was also mapped using a force balance as a function of angle-of-attack. Further details on the water-channel and PIV set-up can be found in (Zhao et al., 2018). Results are shown here for the channel velocity of the velocity 0.17 m/s corresponding to the Reynolds number $Re = 5000$.

The time-averaged lift coefficients are shown with grey dots in Fig. 1 (a). For angles $\alpha < 7.75^\circ$, we observe a rather good agreement with results of the two-dimensional simulations (black dots), while for larger angles of attack $\alpha \geq 7.75^\circ$, the discrepancy is more pronounced. The existence of hysteresis was also explored experimentally by gradually increasing and then gradually decreasing the angle of attack. This is also visible in Fig. 1 (a) with two (light grey) circles are visible for each angle.

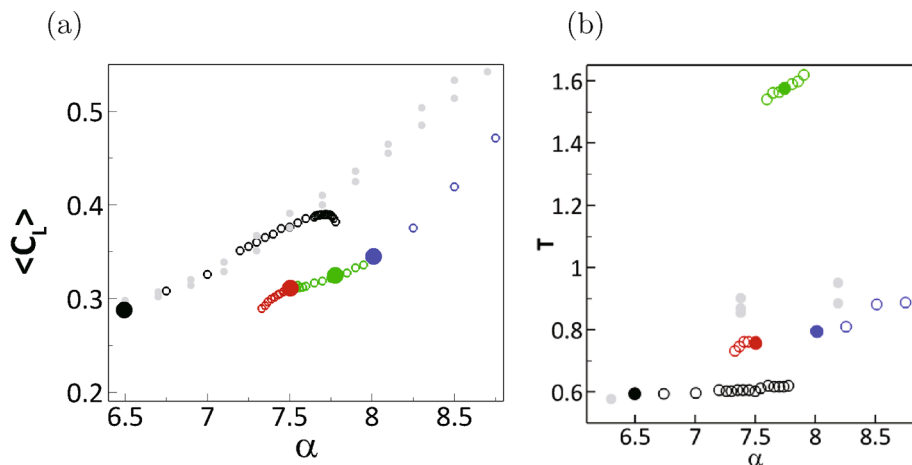


Fig. 1. (a) Time-averaged lift coefficient ($\langle C_L \rangle$), and (b) period T of the lift coefficient, as a function of α , for $Re = 5000$. The four branches of numerical periodic solutions are identified by black, red, green and blue open circles. Large filled circles identify solutions displayed in subsequent figures. The experimental results are shown with grey dots.

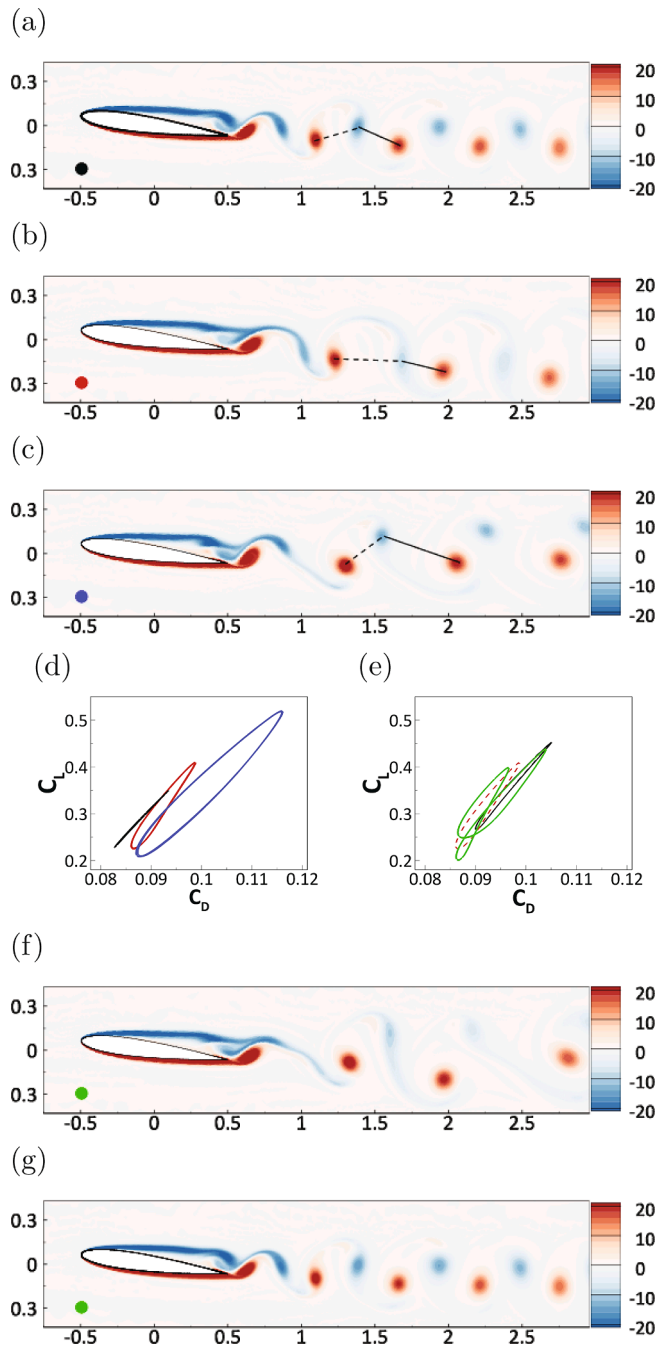


Fig. 2. Isocontours of the instantaneous vorticity for the periodic solutions at (a) $\alpha = 6.5^\circ$, (b) $\alpha = 7.5^\circ$, (c) $\alpha = 8^\circ$, and (f,g) $\alpha = 7.75^\circ$ for times corresponding to the maximal lift. Their temporal evolution in instantaneous lift-versus-drag coefficients diagrams is displayed with solid curves in (d) for $\alpha = 6.5^\circ$ (black,a), 7.5° (red,b) and 8° (blue,c), and in (e) for $\alpha = 7.75^\circ$. In (e), the dashed curves correspond to trajectories for $\alpha = 7.5^\circ$ for the high-lift (black) and low-lift (red) solutions.

These slightly different values are attributed to measurement errors and do not correspond to different flow solutions. Therefore, no evidence of flow hysteresis has been found in the experiments for the explored range of attack. Considering now the unsteady behaviour, we identified a dominant peak for the power spectral density of the lift coefficients at frequencies f_e . The corresponding periods $T = 1/f_e$ are reported in Fig. 1 (b) with grey dots. For the lowest angle, we again observe a good agreement between experimental and numerical results. For larger angles ($\alpha = 7.5^\circ$ and $\alpha = 8.2^\circ$), the experimental frequency slightly

overshoots the numerical prediction obtained for the low-lift solutions. We also note that we did not identify any peak at frequency $f_e/2$, so that a period-doubling bifurcation could not be obtained in the experiments. Fig. 4 shows two instantaneous PIV vorticity plots of the wake as α is increased from 5° to 6° . While the spatial pattern of the vorticity is typical of vortex-shedding at $\alpha = 5^\circ$ (see Fig. 3-a), a change of topology is already observed for $\alpha = 6^\circ$ (see Fig. 4-b), even if the experimental and numerical frequencies were in good agreement for that angle. A change of topology is also observed in the results of the numerical simulations, but for a larger angle of attack $\alpha \sim 7.5^\circ$.

2.3. Discussion

The discrepancies between the experimental and numerical results might be due to a three-dimensional flow transition that cannot be captured with the present two-dimensional numerical simulations. We here further explore that assumption.

The three-dimensional flow transition is better understood for the wake of bluff bodies (Williamson, 1996) than for the wake of airfoils. Briefly, there exists three modes, labelled A, B and C that occur in the wake of a circular cylinder. Mode A (resp. B) is characterized by a wavelength around $\lambda_z = 4d$ (resp. $\lambda_z = 0.8d$) and is observed in experiments (Zhang et al., 1995) for diameter-based Reynolds numbers $Re_d > 200$ (resp. $Re_d > 270$). The mode C is different from modes A and B in the sense that it exhibits period-doubling. Its spanwise wavelength is $2d$.

For the wake of airfoils, the development of three-dimensional structures was simulated in Hoarau et al. (2003, 2006) for a NACA0012 airfoil at Reynolds number $Re = 800$ and angle of attack $\alpha = 20^\circ$. The authors proposed to use the apparent thickness $d = \sin(\alpha)$ for comparing the transverse wavelength of their structure to those usually reported for cylinders. The Reynolds number $Re_d = Re \sin(\alpha)$ based on that apparent thickness can also be used for comparing the Reynolds numbers of airfoils to that of bluff bodies. The spanwise wavelength of their structures is $\lambda_z = 0.64d$ and the equivalent Reynolds number is $Re_d = 273$. This is characteristic of the mode B observed for a cylinder. For the wake of a NACA0015 airfoil, a Floquet stability analysis of the two-dimensional periodic flow allowed to identify the types of Floquet modes getting unstable for several angles of attack (Deng et al., 2017). If a mode B is unstable for angles of attack $\alpha > 17.5$, the authors found that a mode C gets unstable for $\alpha > 12.5$ and $Re \geq 1082$. This Floquet mode being subharmonic, the three-dimensional flow transition thus occurs through a period-doubling bifurcation in this range of angle. More recently, a similar results was also reported for an Eppler 61 airfoil at $\alpha = 10^\circ$ (Samuthira Pandi and Mittal, 2019).

To our knowledge, there is no investigation of the three-dimensional wake flow transition for the NACA0012 at low angles of attack. Therefore, we will use results on the cylinder to estimate the critical angle above which the three-dimensional transition may occur. Assuming that a mode A gets unstable for the same Reynolds number as for the cylinder, i.e. $Re_d = 200$, we obtain that the critical angle of attack is $\alpha = 2.4^\circ$. For the mode B, the critical angle would be $\alpha = 3.1^\circ$ and even lower for the mode C. All of these estimations are well below the angle of attack $\alpha = 6^\circ$ for which we observe a discrepancy between experimental results and two-dimensional numerical simulations, so that the wake flow is probably three-dimensional in the present experiments. Even if the two-dimensional solutions may not be observed in the experiments, we will perform in the next section linear analysis of their time-averaged (mean) flow velocity.

3. Linear analyses of time-averaged flows

In this section, we analyse the time-periodic flows previously described by performing linear analyses of the time-averaged flow. Decomposing the flow velocity and pressure as the sum of the time-averaged flow fields (\bar{u}, \bar{p}) and their fluctuations (u', p') , and inserting

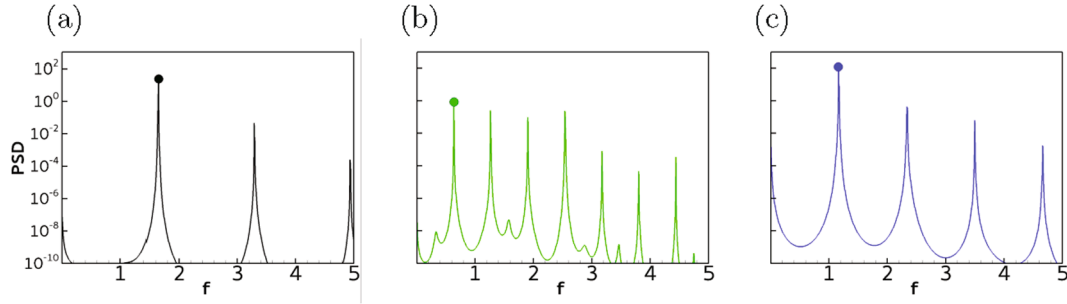


Fig. 3. Power spectral density as a function of the frequency f computed for the lift coefficient for the angles of incidence (a) $\alpha = 6.5^\circ$, (b) $\alpha = 7.75^\circ$ and (c) $\alpha = 8^\circ$. The lowest frequency f_i , marked with circles, is used to compute the period $T = 1/f_i$ displayed in Fig. 1-b.

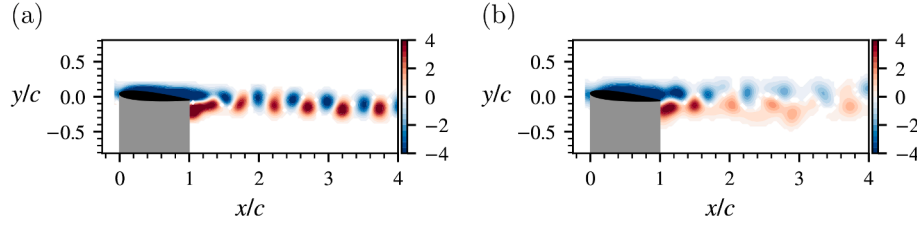


Fig. 4. Experimental results at $Re = 5000$. PIV snapshots (vorticity) showing the change in the wake topology when increasing the angle-of-attack from (a) $\alpha = 5^\circ$ to (b) $\alpha = 6^\circ$.

this decomposition into the governing Eq. (1), one obtains the following exact equations governing the dynamics of the fluctuations:

$$\frac{\partial u'}{\partial t} + (u' \cdot \nabla) \bar{u} + (\bar{u} \cdot \nabla) u' + \nabla p' - \frac{1}{Re} \Delta u' = f', \quad \nabla \cdot u' = 0, \quad (2)$$

where $f' = -(u' \cdot \nabla) u' + \overline{(u' \cdot \nabla) u'}$. This exact equation cannot be solved without a priori knowledge (i) of the mean velocity field \bar{u} and (ii) of the right-hand side forcing f' that represents the effect on the fluctuations of the nonlinear interaction between fluctuations. Nevertheless, it allows to distinguish between two sources of nonlinearity and how they impact the dynamics of fluctuations. The first source of nonlinearity is the mean flow, since it results from the nonlinear interaction between fluctuations via the Reynolds stress tensor. Its effect on the fluctuations is however linear since the left-hand side operator is the linearized Navier–Stokes equations around that mean flow. The second source of nonlinearity is the right-hand side forcing term that gathers all the nonlinear interaction between fluctuations, except those already accounted for in the Reynolds stress tensor. This distinction between the two sources of nonlinearity somehow led to two methods for reconstructing the flow fluctuations. The mean-flow eigenvalue and resolvent analyses are presented and applied in the next subsections.

3.1. Mean-flow eigenvalue analysis

Neglecting the right-hand side forcing f' in the above equation, the flow perturbation $q' = (u', p')$ is decomposed in the form $q' = \tilde{q}(x) \exp(\sigma t) + c.c.$, where $\tilde{q}(x)$ are complex spatial structures, known as global modes, whose temporal behaviour is given by the complex scalar $\sigma = \lambda + i\omega$. Injecting that decomposition into (2) yields the eigenvalue problem

$$(\sigma M - L(\bar{u})) \tilde{q} = 0, \quad (3)$$

where L denotes the discrete Navier–Stokes equations linearized around the mean flow velocity field \bar{u} and M is a mass matrix. In the mean-flow eigenvalue analysis proposed by (Barkley, 2006), we look for leading eigenmodes that are marginal, i.e. their growth rate $\lambda \sim 0$.

We performed the eigenvalue analysis using mean flows of the pe-

riodic solutions reported in the previous section for several angles of attack. The mean flows are shown in Fig. 5 while the corresponding eigenvalue spectra are displayed in Fig. 6. We note that all the eigenvalues are stable ($\lambda < 0$) indicating that, for all angles of attack, the mean flow is stable. This is slightly different from the result by Barkley who obtained a slightly unstable mode. Because the mean flow is stable in the present case, we may legitimately argue that a right-hand side forcing term should be included so as to sustain fluctuations. This clearly

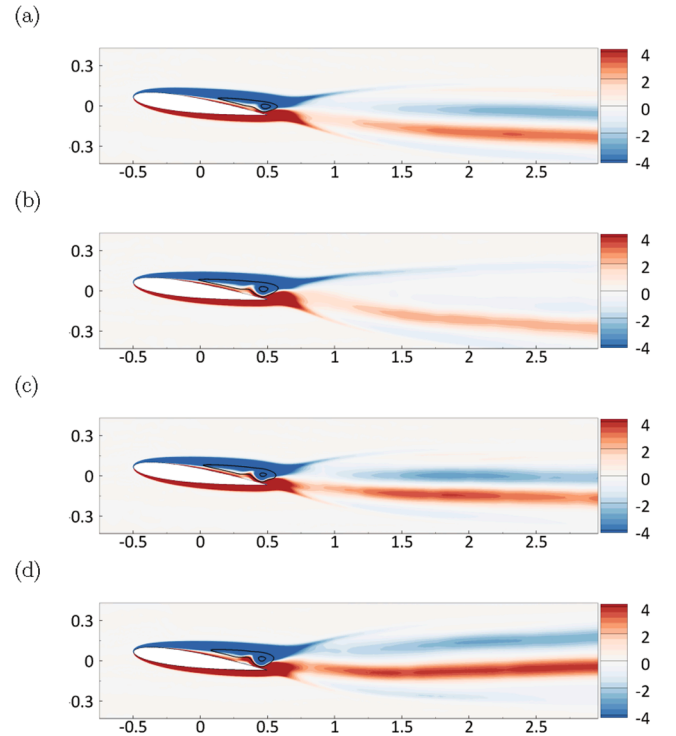


Fig. 5. Vorticity field of the mean flow computed for (a) $\alpha = 6.5^\circ$, (b) $\alpha = 7.5^\circ$ (high-lift branch), (c) $\alpha = 7.5^\circ$ (low-lift branch, red) and (d) $\alpha = 8^\circ$. The black curves are streamlines indicating the recirculation region.

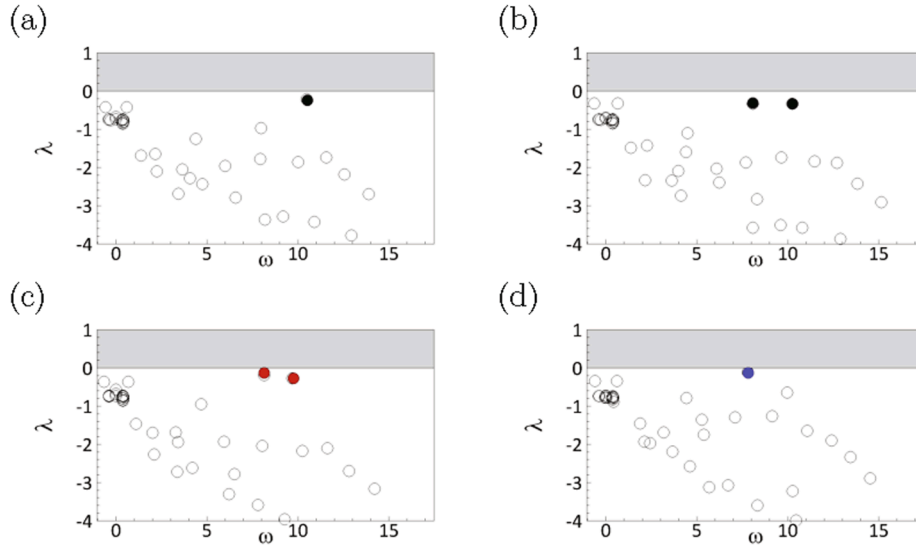


Fig. 6. Eigenvalue spectra obtained for the time-averaged flow solutions at (a) $\alpha = 6.5^\circ$, (b) $\alpha = 7.5^\circ$ (high-lift branch), (c) $\alpha = 7.5^\circ$ (low-lift branch, red) and (d) $\alpha = 8^\circ$.

favors the resolvent analysis of the mean flow that will be presented in the next subsection. Before doing so, it is still interesting to further examine the eigenvalue spectra. For the angle of attack $\alpha = 6.5^\circ$ (Fig. 3-a), there exists one eigenvalue close to be unstable at the (circular) frequency $\omega = 10$. The corresponding frequency $f = \omega/(2\pi) = 1.6$ is very close to the vortex-shedding frequency reported in the temporal simulations (see Fig. 3-a). When increasing the angle to $\alpha = 7.5^\circ$, two mean flows may be considered corresponding to the high-lift periodic solution (black curve in Fig. 1) and low-lift periodic solutions (red curve). Fig. 6(b) and 6(c) shows the eigenvalue spectra obtained for these high-lift and low-lift solutions, respectively. Interestingly, we observe in both cases the existence of two modes close to be unstable. The frequency of the highest-frequency mode is close to the frequency of the high-lift solution, while that of the lowest-frequency mode is close to the low-lift solution. When further increasing the angle up to $\alpha = 8^\circ$ for which only the low-lift solutions exists (blue curve in Fig. 1), the highest-frequency mode is stabilized (Fig. 6-d) while the lowest-frequency mode remains close to be marginally stable. The existence of those two quasi-marginal modes is limited to angles for which a hysteresis of periodic solutions is observed. To conclude that subsection, we comment results obtained for the mean flow computed from the period-doubling solution, not shown here. They are very similar to those displayed in Fig. 6(b) and (c). Therefore, we did not find any quasi-marginal mode whose frequency is half the frequency of the vortex-shedding, i.e. $\omega \sim 4-5$. Thus, the period-doubling bifurcation cannot be explained with a mean flow analysis. While a Floquet analysis of the periodic base flow might explain its emergence, since it takes into account the interaction of fluctuation with all harmonics of the periodic base solution, it requires the knowledge of the unstable time-periodic flow, that cannot be computed with temporal simulations. For the reader interested by computing unstable periodic solutions, we refer to (Jallas et al., 2017; Shaabani-Ardali et al., 2017).

3.2. Mean-flow resolvent analysis

As concluded from the mean-flow eigenvalue analysis previously performed, the right-hand side forcing term f' in (2) cannot be entirely neglected in order to sustain the fluctuations. In the mean-flow resolvent analysis, this non-linear term is modelled as an external unknown forcing, yielding a linear relationship between the velocity field response and this nonlinearity (McKeon and Sharma, 2010). The Fourier decomposition of the fluctuation and forcing, i.e. $(q', f')(x, t) =$

$(\hat{q}, \hat{f})(x)\exp(i\omega t) + c.c.$, is injected into the Eqs. (2), yielding the linear input–output harmonic equation,

$$(i\omega M - L(\bar{u}))\hat{q} = MP\hat{f}, \quad (4)$$

where P is a rectangular matrix introduced to prolongate the momentum forcing vector onto a vector of size \hat{q} . The transpose of this matrix allows extracting the velocity vector from the flow vector, i.e. $\hat{u} = P^T\hat{q}$. The resolvent operator $R(\omega)$ is often introduced as follows,

$$\hat{u} = P^T(i\omega M - L(\bar{u}))^{-1}MP\hat{f} = R(\omega)\hat{f}, \quad (5)$$

to express the linear relationship between the output harmonic velocity \hat{u} and the input harmonic forcing \hat{f} . The resolvent modes are the left (response) and right (forcing) modes in a singular value decomposition of the resolvent operator. The forcing modes \tilde{f}_k may be obtained by computing the eigenmodes for the following Hermitian eigenvalue problem

$$(R(\omega)^H R(\omega))\tilde{f}_k = \lambda_k^2 \tilde{f}_k. \quad (6)$$

The response modes \tilde{u}_k are then obtained as the solution of (4) with $\tilde{f} = \tilde{f}_k$. Assuming that the forcing modes are normalised as $\tilde{f}_k^H M \tilde{f}_k = 1$, the kinetic energies of the response modes correspond to the positive eigenvalues of the above eigenvalue problem, i.e. $\lambda_k^2 = \tilde{u}_k^H M \tilde{u}_k$. Ranking the eigenmodes in decreasing order of kinetic energy ($\lambda_0^2 > \lambda_1^2 > \dots$), the leading modes (of largest energy gain) have been used to reconstruct the flow fluctuations (see for instance Beneddine et al., 2017).

The resolvent analysis is first performed for the mean-flow of the periodic solution at $\alpha = 6.5^\circ$ displayed in Fig. 2(a). Fig. 7(a) shows the energy gain of the leading modes as a function of the forcing period $2\pi/\omega$. A peak is clearly observed around the forcing period 0.61, close to the flow period of 0.6. This peak is clearly related to the proximity of the eigenvalue (black dot) in Fig. 6(a) to the real axis. The real part of the resolvent mode corresponding to that forcing period is displayed in Fig. 8(a) with isocontours of vorticity. The oscillating pattern in the streamwise direction is typical of vortex shedding. However, a comparison with the pattern of the fundamental harmonic of the periodic solution, shown in Fig. 8(b), reveals different shapes in the cross-stream direction, the latter being more spread. For that angle-of-attack, the resolvent analysis well identifies the oscillating frequency of the periodic solution, but it does not perfectly capture the spatial structure of the

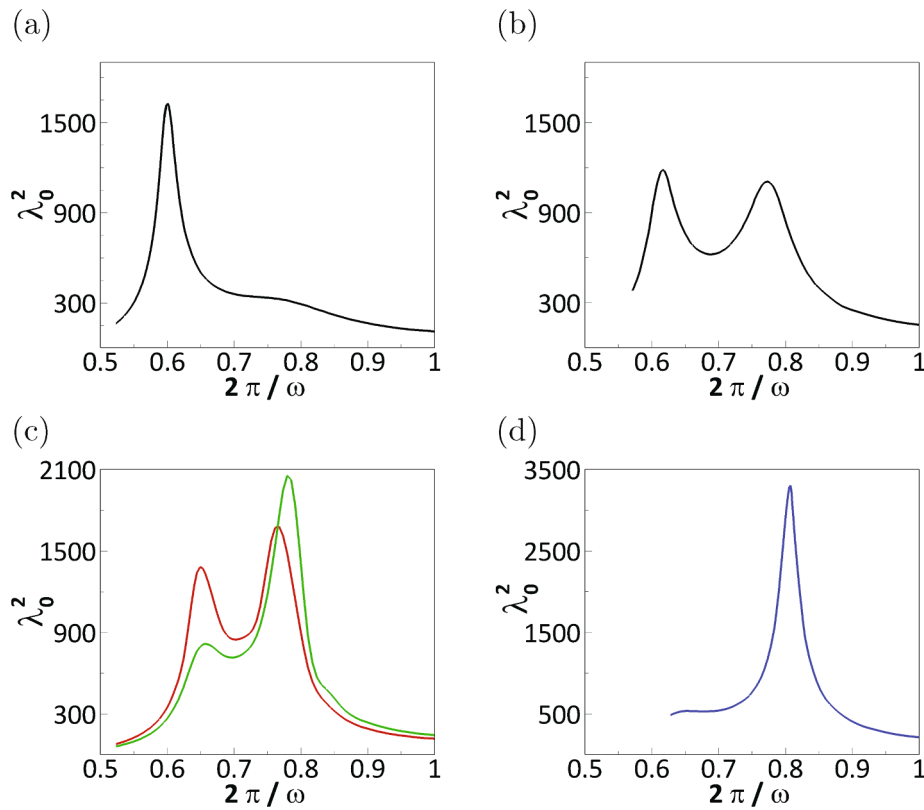


Fig. 7. Resolvent analysis of the time-averaged flow solutions for (a) $\alpha = 6.5^\circ$, (b) $\alpha = 7.5^\circ$ (high-lift branch), (c) $\alpha = 7.5^\circ$ (low-lift branch, red) and $\alpha = 7.75^\circ$ (low-lift branch, green), and (d) $\alpha = 8^\circ$. The energetic gain λ_0^2 of the leading resolvent modes is displayed as a function of the forcing period $2\pi/\omega$.

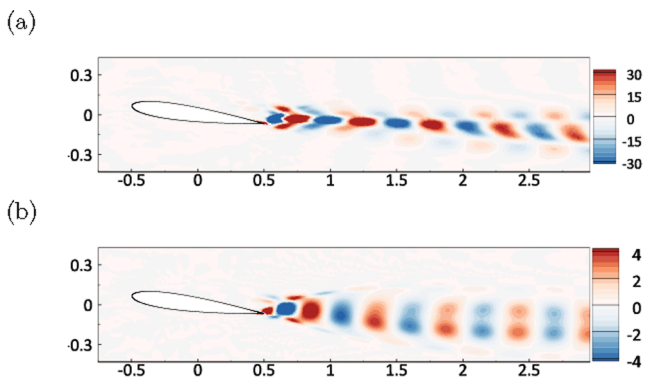


Fig. 8. Streamwise vorticity of (a) the resolvent mode, and (b) the fundamental harmonic of the periodic flow at $\alpha = 6.5^\circ$. The resolvent mode corresponds to the energy peak in Fig. 7(a) for the forcing period $2\pi/\omega = 0.61$. The fundamental harmonic oscillates at period $T = 0.6$.

fundamental harmonic.

We now turn to results of the resolvent analysis performed for the angle-of-attack $\alpha = 7.5^\circ$, for which we recall that two periodic solutions co-exist, a high-lift solution (black circles) in Fig. 1 and a low-lift solution (red circles). The energy gains are displayed in Fig. 7(b) and (c), respectively, identified by the same colors. Although both solutions are periodic (and thus characterised by one fundamental frequency), we observe two peaks in the resolvent analysis (in both cases). Again, the existence of these two peaks is related to the existence of two eigenvalues close to the real axis in Fig. 6(b). The first one is obtained for the forcing period $2\pi/\omega = 0.6 - 0.65$ and is close to the period of the high-lift periodic solution. The second peak obtained for the forcing period $2\pi/\omega = 0.76 - 0.78$ is close to the period of the low-lift periodic solution.

These two peaks are also obtained for the resolvent analysis of the doubling-period solution (green) and the sum of the forcing period is now close to the flow period $T = 1.6$. No peak of energy is obtained at this forcing period.

These two peaks clearly indicate the existence of two mechanisms of linear amplification, similarly to Symon et al. (2019) for the flow around an airfoil at higher Reynolds number $Re = 10000$ and angle-of-attack $\alpha = 10.5^\circ$. However, in the present case, the two peaks are associated with similar frequencies and related to the amplification of wake instabilities, not to Kelvin–Helmholtz instabilities in the shear layer. Clearly, when the two periodic solutions are getting close in the phase space (see Fig. 2(e)), the resolvent analysis of the mean flow reveals the existence of both linear mechanisms characterising each periodic solution. As noted for $\alpha = 6.5^\circ$, the resolvent response shown in Fig. 9(a) does not perfectly compare to the fundamental harmonic shown in Fig. 9(b). Finally, when increasing the angle-of-attack to $\alpha = 8^\circ$, only the high-frequency peak of energy remains in Fig. 7(d), corresponding to the flow period. The response mode displayed in Fig. 10(a) does not so well approximate the fundamental harmonic shown in Fig. 10(b). This discrepancy is probably due to the higher-harmonics terms (somehow neglected in the resolvent analysis since embedded in the linear forcing f'), that play a role in transferring the energy between different flow harmonics (Jin et al., 2021).

4. Conclusion

Numerical simulations of the two-dimensional flow around a NACA0012 airfoil at $Re = 5000$ show that the wake undergoes a series of bifurcations at relatively low angle of incidence $6^\circ < \alpha < 8^\circ$. Periodic solutions with close frequencies may coexist and a solution branch showing period-doubling is also identified. When the periodic solutions are close in the phase space, a resolvent analysis of their mean-flow identifies two peaks of energetic amplification, corresponding to the

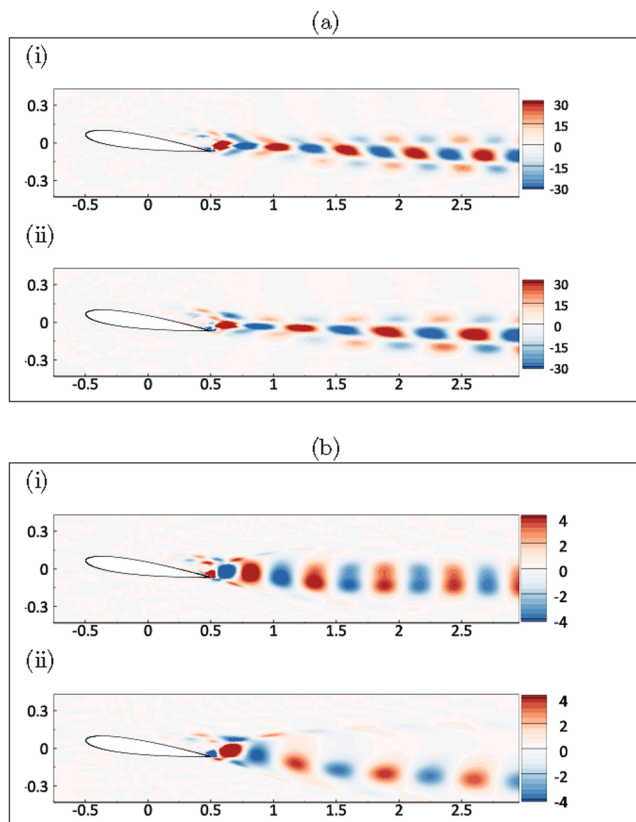


Fig. 9. Streamwise vorticity of (a) the resolvent mode of the high-lift periodic solution, and (b) the fundamental harmonics of the high-lift (top) and low-lift (bottom) periodic solutions at $\alpha = 7.5^\circ$. The resolvent modes in (a) corresponds to the two energy peaks in Fig. 7(b) for the forcing period (top) $2\pi/\omega = 0.61$ and (bottom) $2\pi/\omega = 0.76$. The fundamental harmonics in (b) oscillate at the periods (top) $T = 0.61$ and (bottom) $T = 0.76$.

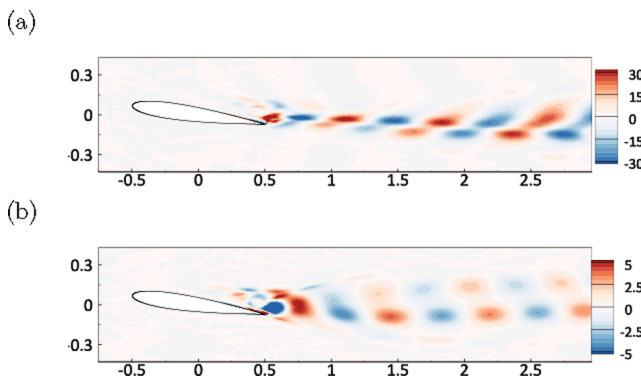


Fig. 10. Streamwise vorticity of (a) the resolvent mode, and (b) the fundamental harmonic of the periodic flow at $\alpha = 8^\circ$. The resolvent mode corresponds to the energy peak in Fig. 7(d) for the forcing period $2\pi/\omega = 0.81$. The fundamental harmonic oscillates at period $T = 0.8$.

frequencies of both periodic solutions.

Finally, the experimental results suggest that the flow undergoes a three-dimensional transition at an angle-of-attack of $\alpha \sim 6^\circ$ that does not much influence the time-averaged lift coefficient up to $\alpha \sim 8^\circ$. The existence of hysteresis was also explored experimentally by gradually increasing and then gradually decreasing the angle of attack; however, no evidence has been found of this so far. It would be interesting to explore this aspect further by evolving the two-dimensional flow three-dimensionally from the lower branch of Fig. 1(a) to a fully saturated

state, and also to undertake resolvent analysis on the mean three-dimensional wake(s). This will be pursued in a subsequent study.

CRediT authorship contribution statement

O. Marquet: Conceptualization, Methodology, Software, Visualization, Writing - original draft, Funding acquisition. **J.S. Leontini:** Conceptualization, Methodology, Validation, Writing - review & editing. **J. Zhao:** Conceptualization, Visualization, Investigation, Writing - review & editing. **M.C. Thompson:** Conceptualization, Methodology, Validation, Writing - review & editing, Funding acquisition.

Declaration of Competing Interest

The authors declare that they have no known competing financial interests or personal relationships that could have appeared to influence the work reported in this paper.

Acknowledgements

This project has received funding from the European Research Council (ERC) under the European Union Horizon 2020 Research and Innovation Program (grant agreement 638307), and was also supported by Australian Research Council (ARC) Discovery grants DP190103388 and DE200101650.

References

- Alam, M.M., Zhou, Y., Yang, H., Guo, H., Mi, J., 2010. The ultra-low reynolds number airfoil wake. *Experiments in fluids* 48 (1), 81–103.
- Alizard, F., Cherubini, S., Robinet, J.-C., 2009. Sensitivity and optimal forcing response in separated boundary layer flows. *Physics of Fluids* 21 (6), 064108.
- Barkley, D., 2006. Linear analysis of the cylinder wake mean flow. *EPL (Europhysics Letters)* 75 (5), 750.
- Beneddine, S., Yegavian, R., Sipp, D., Leclaire, B., 2017. Unsteady flow dynamics reconstruction from mean flow and point sensors: an experimental study. *Journal of Fluid Mechanics* 824, 174.
- Deng, J., Sun, L., Shao, X., 2017. Floquet stability analysis in the wake of a naca0015 airfoil at post-stall angles of attack. *Physics of Fluids* 29 (9), 094104.
- Hoarau, Y., Braza, M., Ventikos, Y., Faghani, D., Tzabiras, G., 2003. Organized modes and the three-dimensional transition to turbulence in the incompressible flow around a naca0012 wing. *Journal of Fluid Mechanics* 496, 63–72.
- Hoarau, Y., Braza, M., Ventikos, Y., Faghani, D., 2006. First stages of the transition to turbulence and control in the incompressible detached flow around a naca0012 wing. *International journal of heat and fluid flow* 27 (5), 878–886.
- Huang, R.F., Lin, C.L., 1995. Vortex shedding and shear-layer instability of wing at low-reynolds numbers. *AIAA journal* 33 (8), 1398–1403.
- Huang, R., Wu, J., Jeng, J., Chen, R., 2001. Surface flow and vortex shedding of an impulsively started wing. *Journal of Fluid Mechanics* 441, 265–292.
- Jallas, D., Marquet, O., Fabre, D., 2017. Linear and nonlinear perturbation analysis of the symmetry breaking in time-periodic propulsive wakes. *Physical Review E* 95 (6), 063111.
- Jin, B., Symon, S., Illingworth, S.J., 2021. Energy transfer mechanisms and resolvent analysis in the cylinder wake. *Physical Review Fluids* 6 (2), 024702.
- John, V., et al., 2016. *Finite element methods for incompressible flow problems*. Springer.
- Kurtulus, D.F., 2016. On the wake pattern of symmetric airfoils for different incidence angles at $re = 1000$. *International Journal of Micro Air Vehicles* 8 (2), 109–139.
- Malkus, W., 1956. Outline of a theory of turbulent shear flow. *Journal of Fluid Mechanics* 1 (5), 521–539.
- Mantić-Lugo, V., Gallaire, F., 2016. Self-consistent model for the saturation mechanism of the response to harmonic forcing in the backward-facing step flow. *Journal of Fluid Mechanics* 793, 777–797.
- Mantić-Lugo, V., Arratia, C., Gallaire, F., 2015. A self-consistent model for the saturation dynamics of the vortex shedding around the mean flow in the unstable cylinder wake. *Physics of Fluids* 27 (7), 074103.
- Marquet, O., Sipp, D., 2010. Global sustained perturbations in a backward-facing step flow. In: *Seventh IUTAM Symposium on Laminar-Turbulent Transition*. Springer, pp. 525–528.
- Marquet, O., Sipp, D., 2012. Convective instabilities in a backward-facing step flow: global forced perturbations, *Progress in Flight. Physics* 3, 451–460.
- McKeon, B.J., Sharma, A.S., 2010. A critical-layer framework for turbulent pipe flow. *Journal of Fluid Mechanics* 658, 336–382.
- Mueller, T.J., DeLaurier, J.D., 2003. *Aerodynamics of small vehicles. Annual review of fluid mechanics* 35 (1), 89–111.
- L. Petricca, P. Ohlckers, C. Grinde, Micro- and nano-air vehicles: State of the art, *International journal of aerospace engineering* 2011.

- Pulliam, T.H., Vastano, J.A., 1993. Transition to chaos in an open unforced 2d flow. *Journal of Computational Physics* 105 (1), 133–149.
- Samuthira Pandi, J.S., Mittal, S., 2019. Wake transitions and laminar separation bubble in the flow past an eppler 61 airfoil. *Physics of Fluids* 31 (11), 114102.
- Shaabani-Ardali, L., Sipp, D., Lesshafft, L., 2017. Time-delayed feedback technique for suppressing instabilities in time-periodic flow. *Physical Review Fluids* 2 (11), 113904.
- Sipp, D., Lebedev, A., 2007. Global stability of base and mean flows: a general approach and its applications to cylinder and open cavity flows. *Journal of Fluid Mechanics* 593, 333–358.
- Sipp, D., Marquet, O., 2013. Characterization of noise amplifiers with global singular modes: the case of the leading-edge flat-plate boundary layer. *Theoretical and Computational Fluid Dynamics* 27 (5), 617–635.
- Sipp, D., Marquet, O., Meliga, P., Barbagallo, A., 2010. Dynamics and control of global instabilities in open-flows: a linearized approach. *Applied Mechanics Reviews* 63 (3).
- Stuart, J.T., 1958. On the non-linear mechanics of hydrodynamic stability. *Journal of Fluid Mechanics* 4 (1), 1–21.
- Symon, S., Sipp, D., McKeon, B.J., 2019. A tale of two airfoils: resolvent-based modelling of an oscillator versus an amplifier from an experimental mean. *Journal of Fluid Mechanics* 881, 51–83.
- Thomareis, N., Papadakis, G., 2018. Resolvent analysis of separated and attached flows around an airfoil at transitional Reynolds number. *Physical Review Fluids* 3 (7), 073901.
- Thompson, M.C., Hourigan, K., Cheung, A., Leweke, T., 2006. Hydrodynamics of a particle impact on a wall. *Applied Mathematical Modelling* 30 (11), 1356–1369.
- Turton, S.E., Tuckerman, L.S., Barkley, D., 2015. Prediction of frequencies in thermosolutal convection from mean flows. *Physical Review E* 91 (4), 043009.
- Wang, S., Zhou, Y., Alam, M.M., Yang, H., 2014. Turbulent intensity and reynolds number effects on an airfoil at low reynolds numbers. *Physics of Fluids* 26 (11), 115107.
- Williamson, C., 1996. Three-dimensional wake transition. *Journal of Fluid Mechanics* 328, 345–407.
- Yeh, C.-A., Taira, K., 2019. Resolvent-analysis-based design of airfoil separation control. *Journal of Fluid Mechanics* 867, 572–610.
- Yeh, C.-A., Benton, S.I., Taira, K., Garmann, D.J., 2020. Resolvent analysis of an airfoil laminar separation bubble at $re=500\,000$. *Physical Review Fluids* 5 (8), 083906.
- Zhang, H.-Q., Fey, U., Noack, B.R., König, M., Eckelmann, H., 1995. On the transition of the cylinder wake. *Physics of Fluids* 7 (4), 779–794.
- Zhao, J., Lo Jacono, D., Sheridan, J., Hourigan, K., Thompson, M.C., 2018. Experimental investigation of in-line flow-induced vibration of a rotating circular cylinder. *Journal of Fluid Mechanics* 847, 664–699.
- Zhou, Y., Alam, M.M., Yang, H., Guo, H., Wood, D., 2011. Fluid forces on a very low reynolds number airfoil and their prediction. *International Journal of Heat and Fluid Flow* 32 (1), 329–339.